

ON THE “EXTENDED” SOLAR CYCLE IN CORONAL EMISSION

E. ROBBRECHT¹, Y.-M. WANG, N. R. SHEELEY, JR., AND N. B. RICH²

Space Science Division, Naval Research Laboratory, Washington, DC 20375-5352, USA; eva.robbrecht@oma.be, yi.wang@nrl.navy.mil,
neil.sheeley@nrl.navy.mil, nathan.rich@nrl.navy.mil

Received 2010 February 17; accepted 2010 April 19; published 2010 May 21

ABSTRACT

Butterfly diagrams (latitude–time plots) of coronal emission show a zone of enhanced brightness that appears near the poles just after solar maximum and migrates toward lower latitudes; a bifurcation seems to occur at sunspot minimum, with one branch continuing to migrate equatorward with the sunspots of the new cycle and the other branch heading back to the poles. The resulting patterns have been likened to those seen in torsional oscillations and have been taken as evidence for an extended solar cycle lasting over ~ 17 yr. In order to clarify the nature of the overlapping bands of coronal emission, we construct butterfly diagrams from green-line simulations covering the period 1967–2009 and from 19.5 nm and 30.4 nm observations taken with the Extreme-Ultraviolet Imaging Telescope during 1996–2009. As anticipated from earlier studies, we find that the high-latitude enhancements mark the footpoint areas of closed loops with one end rooted outside the evolving boundaries of the polar coronal holes. The strong underlying fields were built up over the declining phase of the cycle through the poleward transport of active-region flux by the surface meridional flow. Rather than being a precursor of the new-cycle sunspot activity zone, the high-latitude emission forms a physically distinct, U-shaped band that curves upward again as active-region fields emerge at midlatitudes and reconnect with the receding polar-hole boundaries. We conclude that the so-called extended cycle in coronal emission is a manifestation not of early new-cycle activity, but of the poleward concentration of old-cycle trailing-polarity flux by meridional flow.

Key words: Sun: activity – Sun: corona – Sun: dynamo – Sun: magnetic topology – sunspots – Sun: surface magnetism

1. INTRODUCTION

The Fe XIV 530.3 nm green line, whose emissivity peaks near 2 MK, has been used routinely since the 1940s to observe large-scale coronal structures above the solar limb. As summarized by Billings (1966), green-line emission is particularly intense around active regions, with large maxima appearing in the vicinity of, and migrating with, the sunspot latitudes. In addition, weaker maxima are often seen at high latitudes. These secondary maxima migrate poleward during the rising phase of the sunspot cycle (before polar field reversal), but drift equatorward during the declining phase. The green-line emission is found to be more closely correlated with plages and faculae than with sunspots themselves. Plages and faculae in turn are associated with strong network magnetic fields.

The origin of the high-latitude enhancements, which are also seen at many other wavelengths, now appears to be reasonably well understood. In particular, Sheeley et al. (1989) noted that when midlatitude active regions emerged during the rising phase of cycle 22, the nearby polar-hole boundary receded, leaving a band of enhanced He I 1083.0 nm network. They showed that the enhancements occurred at the footpoints of field lines that were previously open but had now become connected (via interchange reconnection) to the trailing-polarity sector of the active region; the high-latitude footpoints represented areas of relatively strong field that had been transported poleward from the sunspot belts over the previous cycle. Subsequently, Wang et al. (1997) used an empirical scaling law to model the green-line emission observed with the Large Angle and Spectrometric Coronagraph (LASCO) on the *Solar and Heliospheric Observatory* (*SOHO*). They confirmed that the enhanced emission along the polar-hole

boundaries was a result of the poleward concentration of the field (see, e.g., Svalgaard et al. 1978), and that the brightest emission came from loops whose lower-latitude ends were rooted in active regions. Benevolenskaya et al. (2001) reached a similar conclusion from their analysis of images recorded with the Extreme-Ultraviolet Imaging Telescope (EIT) on *SOHO* during 1996–2000.

The long-term evolution of the green-line corona can be studied by averaging the emission at a given height above the limb over longitude and plotting the latitudinal distribution of the emission against time. Such “butterfly diagrams” of coronal emission (see Leroy & Noens 1983; Altrock 1997) show the band of high-latitude emission appearing near the poles just after solar maximum, migrating equatorward through the declining phase of the cycle, and reaching latitude $\sim 40^\circ$ – 50° around solar minimum, when the new-cycle sunspots start to emerge. There then seems to be a bifurcation into a branch that follows the equatorward migration of sunspot activity, and one that curves back upward to the poles. As indicated by the question mark in Figure 1 of Leroy & Noens (1983), however, it is unclear whether the zone of high-latitude emission joins continuously onto the main branch of sunspot activity. It should be noted that, because the emission associated with the sunspot belts is so much brighter than the high-latitude enhancements, considerable “massaging” of the data is required to bring out the latter features in the butterfly diagram. Thus, Altrock (1997) plotted the number of local maxima at a given latitude rather than their brightness, while Leroy & Noens (1983) plotted the standard deviation of the green-line emissivity, minus a latitudinal average of the standard deviation.

The butterfly diagram of coronal emission has been likened to the pattern of torsional oscillations, in which zones moving slightly faster and slower than the average photospheric differential rotation propagate from high latitudes toward the equator

¹ Also at George Mason University, Fairfax, VA 22030, USA.

² Also at Interferometrics, Inc., Herndon, VA 20171, USA.

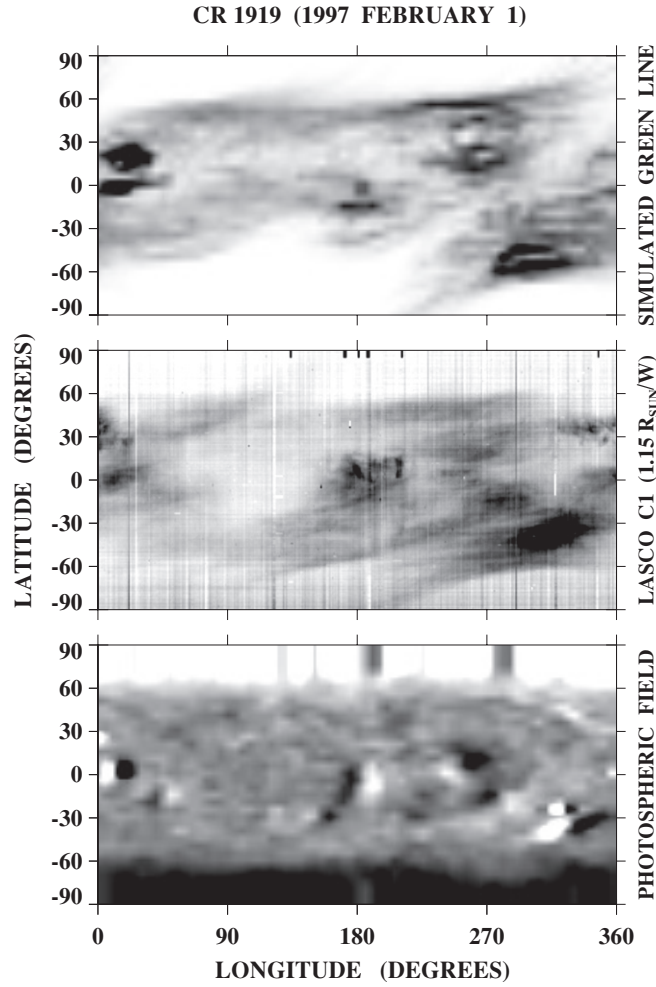


Figure 1. Latitude–longitude maps of green-line emission above the west limb at $r = 1.15 R_{\odot}$ during CR 1919 (starting date 1997 February 1). Top panel: simulation based on a PFSS extrapolation of the MWO photospheric field, a footpoint-density scaling law $n_0 \propto \langle B_0 \rangle / l^{1/2}$, and the assumption of hydrostatic equilibrium at a temperature of 2 MK along closed loops. Gray scale is reversed so that bright (dark) regions are black (white). Middle panel: distribution of 530.3 nm emission observed with the LASCO C1 coronagraph. Bottom panel: underlying MWO photospheric field, with gray scale ranging from $B_r < -8$ G (black) to $B_r > +8$ G (white). Note the steep increase in the field strength toward the poles.

over a period of up to 22 yr (LaBonte & Howard 1982; Leroy & Noens 1983; Snodgrass 1987; Altrock et al. 2008; Howe et al. 2009). The sunspot latitudes lie on the poleward side of the faster zone and on the equatorward side of the slower zone; as illustrated in Figure 1 of Spruit (2003), the amplitude of the velocity deviation correlates with the latitudinal gradient in the photospheric field, not with the field strength itself. It should be emphasized that the torsional oscillations are a second-order effect; the rotation rate itself remains a decreasing function of latitude.

The presence of overlapping bands in the butterfly diagrams of coronal emission and torsional oscillations has often been taken as evidence for an “extended” cycle of solar activity, which begins around the time of polar field reversal and lasts for ~ 17 – 22 yr, propagating from high to low latitudes (see, e.g., Wilson et al. 1988; Legrand & Simon 1981). The high-latitude features that precede the turn-on of sunspots are thus presumed to be the first surface manifestations of the new cycle.

The objective of this study is to clarify the physical nature of the so-called extended cycle in coronal emission, leaving

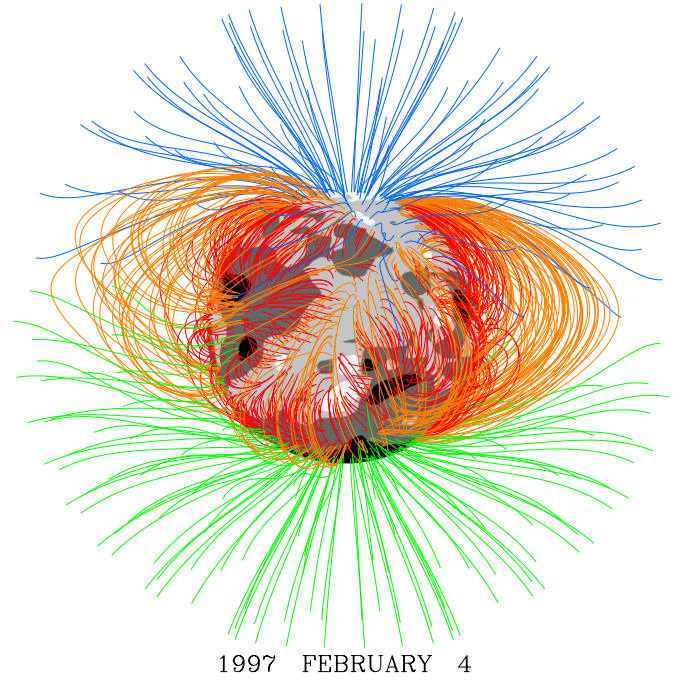


Figure 2. Coronal field-line configuration derived from a PFSS extrapolation of the MWO photospheric field for CR 1919; central meridian is at $\phi = 320^{\circ}$. Closed loops are coded orange if they extend beyond $r = 1.5 R_{\odot}$, red otherwise; open field lines are blue (green) if they have positive (negative) polarity. Black, dark gray, light gray, and white denote areas of the photosphere where the radial field component lies in the ranges $B_r < -6$ G, -6 G $< B_r < 0$ G, 0 G $< B_r < +6$ G, and $B_r > +6$ G, respectively. The active region adjacent to the south polar cap is the same as that located near the bottom right corner of the Carrington maps in Figure 1.

aside the question of whether any relationship exists between this emission and the torsional oscillation patterns. We begin by simulating the evolution of the green-line corona during 1967–2009, applying the scaling-law method of Wang et al. (1997) to the observed photospheric field. The results are displayed in latitude–time format and a physical interpretation of the emission patterns is presented (Section 2). In Section 3, we verify that similar patterns are obtained when the photospheric field measurements are replaced by flux transport simulations in which all of the emerging flux is confined to the sunspot latitudes. In Section 4, we construct butterfly diagrams of Fe XII 19.5 nm and He II 30.4 nm emission using EIT data taken during 1996–2009. Our conclusions are summarized in Section 5.

2. LATITUDE–TIME EVOLUTION OF THE GREEN-LINE CORONA

Our procedure for modeling the green-line corona is similar to that described in Wang et al. (1997). Let n denote the electron density and B the magnetic field strength. The coronal loops are assumed to be in hydrostatic equilibrium at a temperature of 2 MK. The coronal field-line configuration is determined by applying a potential-field source-surface (PFSS) extrapolation to the observed photospheric field; all field lines that extend beyond heliocentric distance $r = R_{ss} = 2.5 R_{\odot}$ are considered to be “open,” with their footpoint areas representing coronal holes. For the magnetograph measurements, we employ synoptic maps from the Mount Wilson Observatory (MWO) for Carrington rotations (CRs) 1516–2088 (1966 December 29 through 2009 October 13). The line-of-sight fields were deprojected by dividing by $\cos L$, where L denotes heliographic latitude, and were

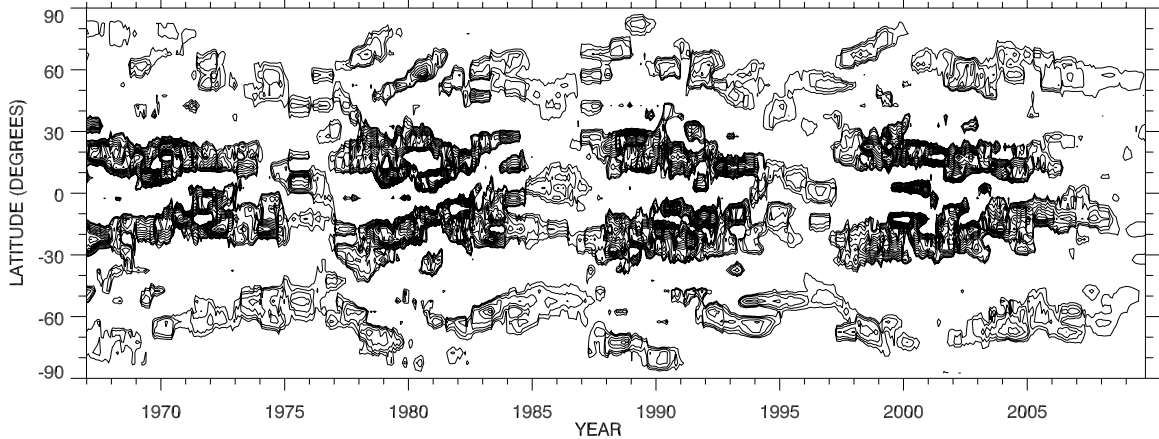


Figure 3. Latitude–time plot of simulated green-line emission at $r = 1.15 R_{\odot}$, spanning the period 1967–2009 (solar cycles 20–23). Here, successive Carrington-format maps like that displayed in the top panel of Figure 1 were averaged over longitude, and an 11 rotation running mean was taken; gray-scale contours show the residual brightness after further subtracting a 25° running mean in latitude. In addition to the equatorward-slanting band of strong emission corresponding to the sunspot belts, a U-shaped band of high-latitude emission is seen in each hemisphere, stretching from one sunspot maximum to the next and centered at sunspot minimum. In most cases, a gap occurs between the bottom of the U and the start of the sunspot activity band.

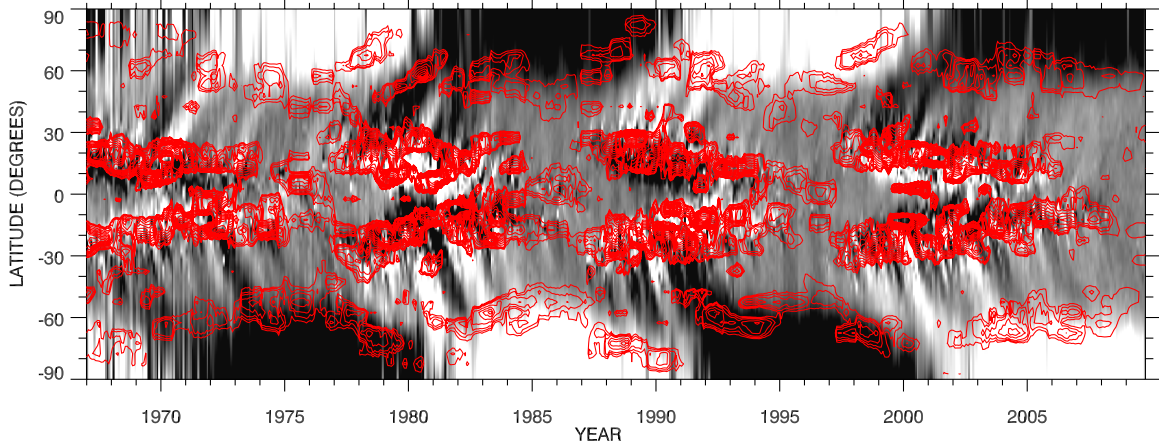


Figure 4. Contours of simulated green-line emission overlaid on a latitude–time plot of the MWO photospheric magnetic field. (The contours are the same as those in Figure 3, but are displayed in red for clarity.) Gray-scale levels for the longitudinally averaged field range from $\langle B_r \rangle_\phi < -4$ G (black) to $\langle B_r \rangle_\phi > +4$ G (white). The high-latitude enhancements are located along the boundaries of the strong polar fields and migrate equatorward and poleward as these fields wax and wane.

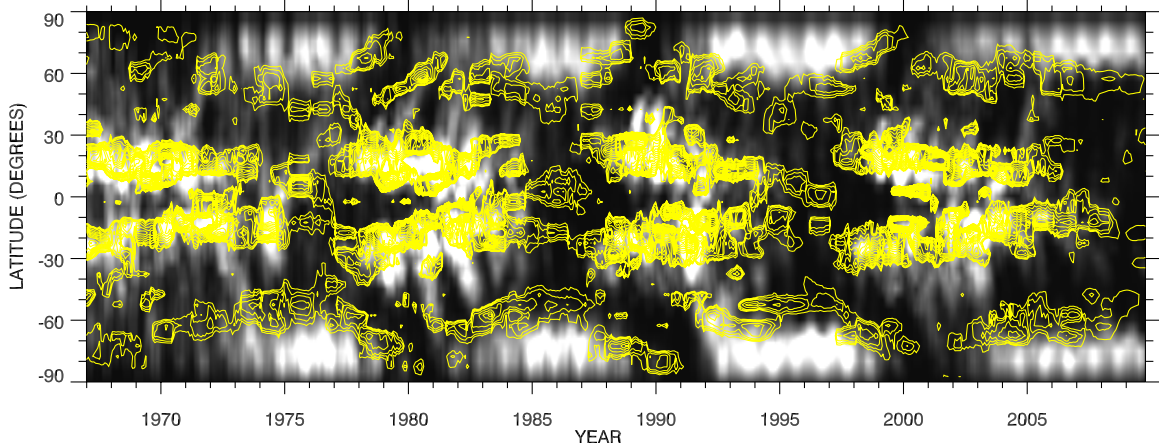


Figure 5. Contours of simulated green-line emission overlaid on a latitude–time plot of the open magnetic flux (coronal holes), derived from a PFSS extrapolation of the MWO photospheric field. (The contours are the same as in Figures 3 and 4, but are here displayed in yellow.) White denotes strong open flux of either polarity; black indicates closed-field regions. The high-latitude enhancements are located just outside the boundaries of the polar coronal holes.

multiplied by $(4.5 - 2.5 \sin^2 L)$ to correct for the saturation of the Fe I 525.0 nm line profile (see Wang & Sheeley 1995; Ulrich et al. 2002, 2009).

The green-line intensity I_{green} is taken to be proportional to the integral of $n^{1.7}$ along the line of sight (see Guhathakurta et al. 1992, 1993), with the contribution from open field lines being

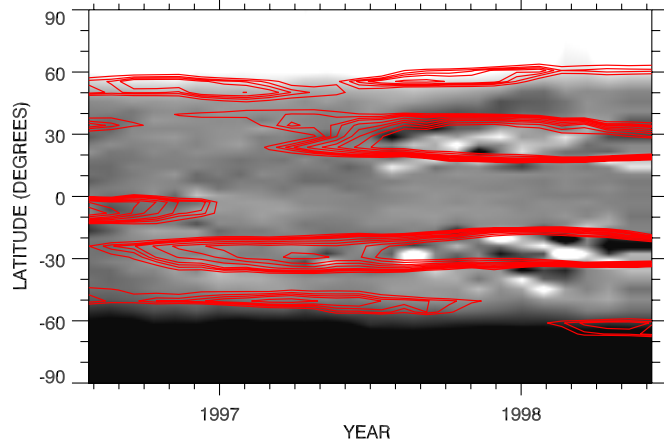


Figure 6. Partial butterfly diagram of observed green-line emission at $r = 1.15 R_{\odot}$ (red contours), constructed by taking five-month running means of LASCO C1 east-limb data recorded during CR 1912–1937 (1996 July through 1998 June). Plotted underneath is the longitudinally averaged photospheric field, with gray-scale levels ranging between $\langle B_r \rangle_\phi < -4$ G (black) and $\langle B_r \rangle_\phi > +4$ G (white). The high-latitude enhancements are seen to form structures distinct from the midlatitude emission bands representing new-cycle active regions.

neglected. The electron density is assumed to obey the scaling law

$$n_0 \propto \langle B_0 \rangle / l^{1/2}, \quad (1)$$

where n_0 is the density at the base of the loop, $\langle B_0 \rangle$ denotes an average of the field strengths at the two footpoints, and l is the loop length. We have found that the results are surprisingly insensitive to the exact form of the scaling law, provided that the electron density is an increasing function of the footpoint field strength.

Our first step is to calculate, at a succession of times as the Sun rotates, the line-of-sight integral of $n^{1.7}$ at a height of $0.15 R_{\odot}$ above the limb, thereby obtaining a latitude–time map of I_{green} for each CR. As an illustrative example, Figure 1 (top panel) shows the simulated map for CR 1919 (starting date 1997 February 1), which is representative of the end of cycle 22 and the onset of cycle 23. For comparison, the middle panel displays the corresponding map assembled from LASCO C1 Fe XIV 530.3 nm images; here, each column of pixels represents a slice of west-limb data taken at $r = 1.15 R_{\odot}$. The underlying photospheric field is shown in the bottom panel. As expected, strong emission occurs above the old- and new-cycle active regions and their remnants. In addition, a ridge of enhanced emission may be seen at high latitudes in each hemisphere, bordering the polar coronal holes. This emission is especially strong on the poleward side of the sheared new-cycle active region located near Carrington longitude $\phi \sim 330^\circ$ in the southern hemisphere. Here, the decaying active region lies so close to the boundary of the south polar hole that its own emission and the high-latitude enhancement effectively merge into a single structure. Figure 2 shows the coronal field-line configuration when the active region is near central meridian; we see that the positive-polarity sector of the active region is linked to the negative-polarity polar cap by closed loops.

Now arranging the 573 simulated green-line maps in sequence and taking an eleven-rotation running mean, we end up with a single map of dimensions 563×36 , in which each pixel represents an average over 5° in latitude and 300 days in time. Without further processing, the map is dominated by the emission from active regions, and resembles the conventional

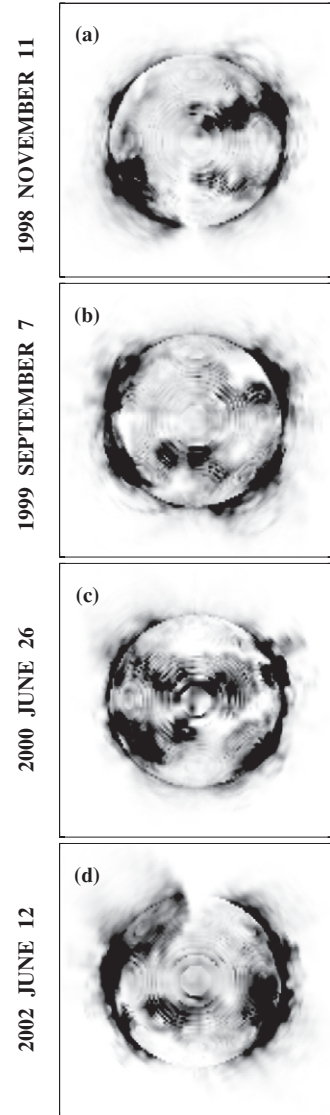


Figure 7. Distribution of simulated green-line emission, as it would appear if it could be seen against the solar disk from Earth, at four representative times during the polar field reversal of solar cycle 23. (a) 1998 November 11. The old-cycle polar holes have shrunk markedly as their flux closes down by connecting to the surrounding midlatitude active regions. (b) 1999 September 7. The polar holes have disappeared and diffuse emission is now present at the poles. (c) 2000 June 26. New-cycle open flux is arriving at the poles, forming lopsided polar holes. (d) 2002 June 12. The new-cycle polar holes are now well established, ringed by enhanced emission from closed loops that connect to leading-polarity flux at lower latitudes.

butterfly diagram for sunspots. In order to bring out the fainter local maxima, we apply an unsharp mask, subtracting from the original map a version that has been smoothed by taking a 25° running mean in latitude. The result is displayed in Figure 3 in the form of a contour plot. Just as in the earlier studies of Leroy & Noens (1983) and Altrock (1997), we find two broad bands of enhanced emission within each hemisphere, one centered on the sunspot belt and the other located at high latitudes. From an inspection of the emission patterns in each hemisphere around the 1976, 1986, and 1996 sunspot minima, it is evident that a gap is usually present between the high-latitude band and the start of the main activity band (the gap is especially pronounced in the southern hemisphere during 1996–1997). On the other hand, the pre- and post-minimum branches of the high-latitude emission tend to form a more continuous, U-shaped structure.

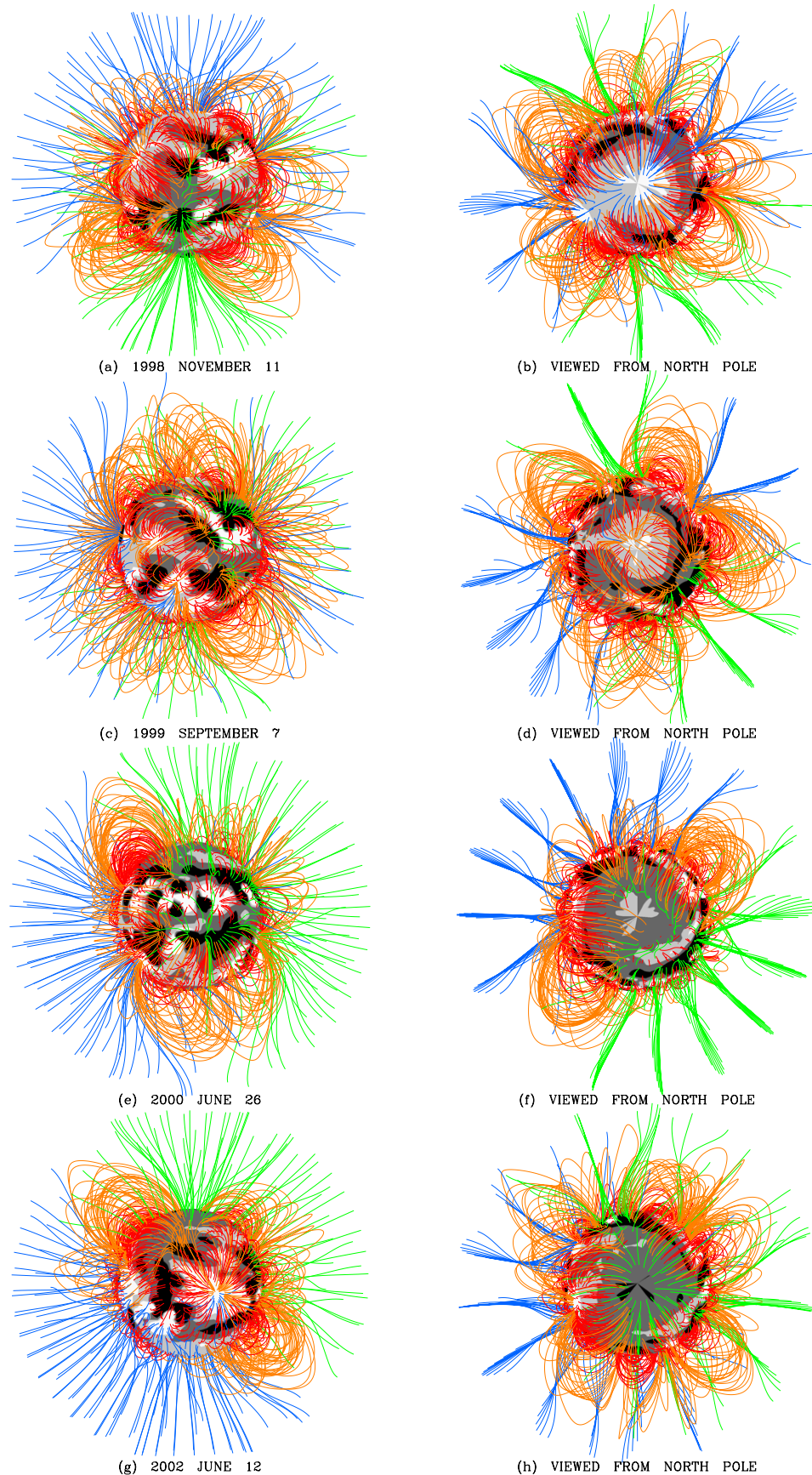


Figure 8. Coronal field-line configurations corresponding to the simulated green-line images of Figure 7. Views from Earth and from above the north pole are displayed at the left and right, respectively. Gray-scale contours for the photospheric field and color coding of the field lines are as in Figure 2.

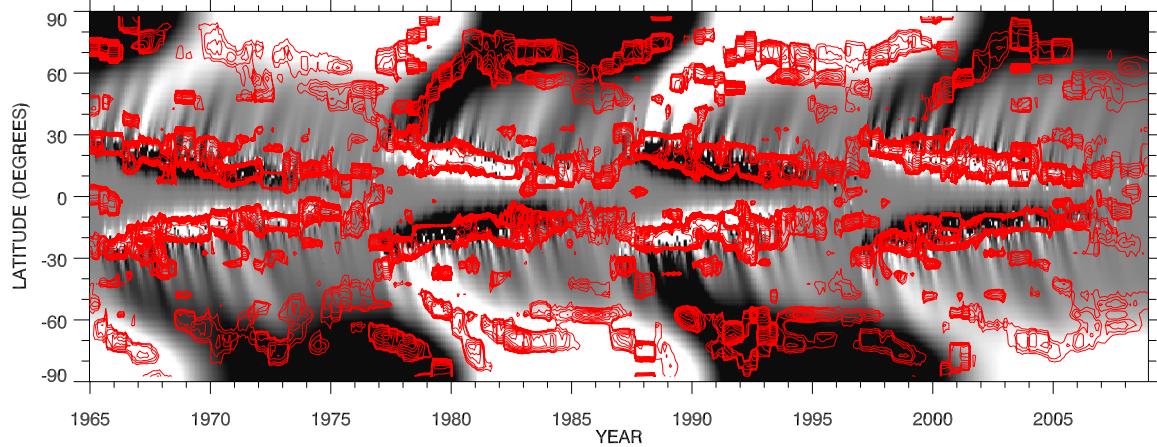


Figure 9. Contours of simulated green-line emission derived from a flux transport simulation of the photospheric field, shown in the underlying latitude–time plot. Here, magnetic bipoles with identical strengths were deposited in the sunspot latitudes at a rate proportional to the observed yearly sunspot numbers during 1965–2008, and evolved including the effects of differential rotation, a $500 \text{ km}^2 \text{ s}^{-1}$ supergranular diffusion, and a $14.5\text{--}17 \text{ m s}^{-1}$ poleward flow, as described in Wang et al. (2009). Gray-scale levels for the simulated photospheric field range from $\langle B_r \rangle_\phi < -4 \text{ G}$ (black) to $\langle B_r \rangle_\phi > +4 \text{ G}$ (white). The resulting patterns of green-line emission are qualitatively very similar to those derived from the MWO photospheric field measurements (compare Figure 4).

Figure 4 places the simulated green-line emission in the context of the evolving solar magnetic field. Here, the emission contours are superimposed on a butterfly diagram of the longitudinally averaged photospheric field $\langle B_r \rangle_\phi$; the gray-scale levels range from $\langle B_r \rangle_\phi < -4 \text{ G}$ (black) to $\langle B_r \rangle_\phi > +4 \text{ G}$ (white). It is apparent that the high-latitude enhancements lie just inside the area defined by the strong polar fields. As the polar fields build up following their reversal near sunspot maximum, and as sunspot activity progresses to lower latitudes, the green-line enhancements likewise migrate equatorward, reaching their lowest latitude of $|L| \sim 45^\circ$ at sunspot minimum; with the onset of new-cycle activity at midlatitudes and the subsequent weakening and cancellation of the polar fields, the enhancements recede poleward again. The waxing and waning of the polar fields is due to the transport, by the surface meridional flow, of trailing-polarity flux from the active regions to the poles. Inspection of Figure 4 reveals, in addition to the high-latitude emission that migrates from midlatitudes to the poles during the rising phase of the cycle, a nearly parallel but more fragmentary band of emission cospatial with the flux that surges to the poles at sunspot maximum. This feature merges with and marks the start of the high-latitude band associated with the new polar fields.

In Figure 5, the green-line contours are overplotted on a butterfly diagram of coronal holes, constructed by applying a PFSS extrapolation to the MWO photospheric field maps and averaging the unsigned open flux over longitude. Here, white indicates latitudes dominated by strong open flux of either polarity, while black denotes areas of closed field. The high-latitude enhancements are seen to lie just outside the boundaries of the polar coronal holes, which advance and recede with the polar fields and extend down to latitude $|L| \sim 60^\circ$ around sunspot minimum.

From Figures 3–5, it can be seen that the high-latitude enhancements underwent a slower equatorward migration during the declining phase of cycle 23 than in cycles 20–22. This slower progression is evidently caused by the failure of the recent polar fields to grow to their previous strength, which in turn led to a shrinking of the polar-hole areas compared with previous cycles (see Kirk et al. 2009; Wang et al. 2009).

Although LASCO C1 green-line observations are available only between mid-1996 and mid-1998, this period lies at

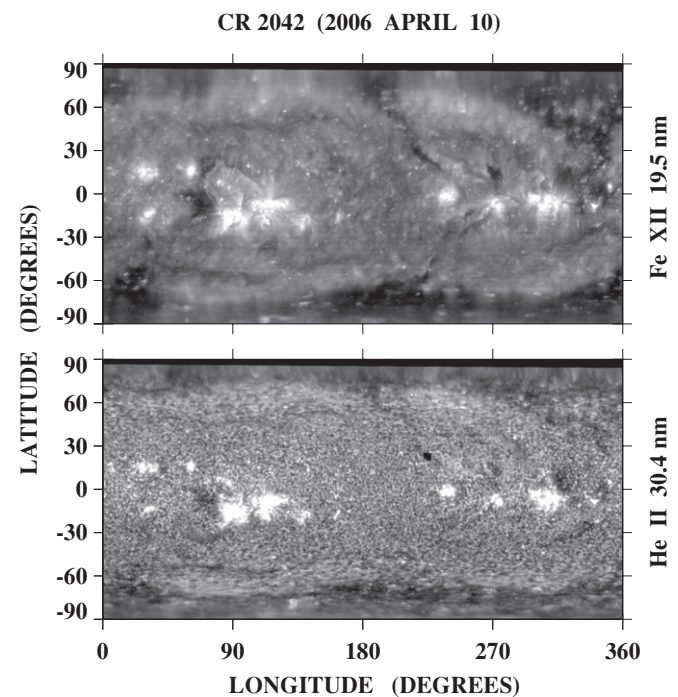


Figure 10. Carrington-format maps showing the distribution of Fe XII 19.5 nm (top panel) and He II 30.4 nm (bottom panel) emission during CR 2042 (starting date 2006 April 10). The maps were assembled from central meridian strips extracted from full-disk SOHO/EIT images. The high-latitude enhancements are clearly seen in both EUV emission lines.

the putative bifurcation point between the high- and low-latitude emission bands. We have therefore constructed a partial butterfly diagram from LASCO C1 530.3 nm maps for CR 1912–1937, and overlaid the results on the longitudinally averaged photospheric field in Figure 6. In deriving the contours of green-line emission, we have employed east-limb data at $r = 1.15 R_\odot$ and taken five-month instead of eleven-month running averages, while subtracting a 25° running mean in latitude as before. The latitude–time plot shows the tail end of the emission band associated with old-cycle active regions near the equator, the emission bands associated with new-cycle active regions emerging at midlatitudes, and the emission bands that run along the equatorward edge of the strong polar-cap

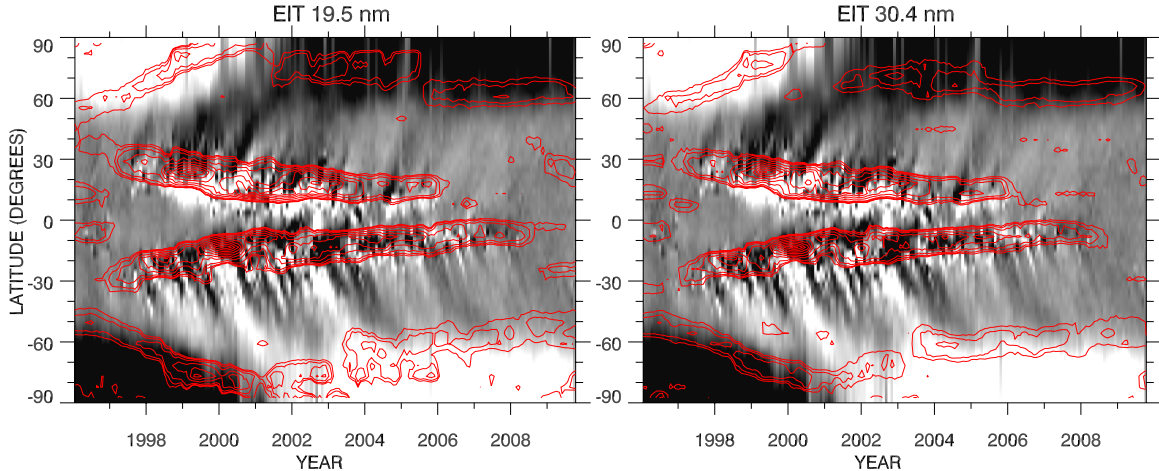


Figure 11. Butterfly diagrams constructed from Fe XII 19.5 nm (left) and He II 30.4 nm (right) EIT synoptic maps spanning solar cycle 23, using the same unsharp mask technique that was applied to the coronal green-line emission. The EUV emission contours are overplotted on the MWO photospheric field. Again, we see a band of high-latitude emission in each hemisphere which is distinct from the main activity zone.

fields. Again, it is evident that the latter enhancements form separate structures from the midlatitude active-region emission, although the two bands approach each other in latitude during this time.

Figure 7 shows full-disk images of simulated green-line emission at four representative times during the polar field reversal of cycle 23. Figure 8 displays the corresponding PFSS-derived coronal field-line configurations, both as seen from Earth (left-hand panels) and as viewed from above the north pole (right-hand panels). On 1998 November 11 (Figures 7(a), 8(a), and 8(b)), the polar holes have shrunk markedly since the onset of the cycle, and the trailing-polarity flux from the new-cycle active regions has formed connections to the remnant polar-cap fields. By 1999 September 7 (Figures 7(b), 8(c), and 8(d)), the polar holes have disappeared and closed loops are now present at the poles, which, however, still have their old-cycle polarity. On 2000 June 26 (Figures 7(c), 8(e), and 8(f)), new-cycle open flux is seen arriving with the trailing-polarity fields in the polar regions, forming lopsided polar holes bounded by loops whose far ends are rooted in leading-polarity flux at lower latitudes. Finally, by 2002 June 12 (Figures 7(d), 8(g), and 8(h)), the new polar holes are fully established, ringed by enhanced emission from large streamer loops.

3. FLUX TRANSPORT SIMULATIONS

In order to confirm that the high-latitude enhancements are associated with flux that has been transported poleward from decayed active regions, and not with flux that has emerged in situ at these latitudes prior to the first sunspots of the next cycle, we show in Figure 9 the green-line contours derived from the flux transport simulations of Wang et al. (2009). Here, the photospheric field has been evolved from 1965 January 1 through 2008 December 31, including the effects of supergranular diffusion, differential rotation, a poleward meridional flow, and flux emergence in the form of bipolar magnetic regions (BMRs). With an initial background field given by $B_r(R_\odot, L, \phi) = -9 \text{ G} \sin^2 L$, the BMRs were deposited in the sunspot belts at random longitudes and at a rate proportional to the yearly mean sunspot numbers, while the meridional flow speed was adjusted from cycle to cycle so as to reproduce the observed variation of the polar fields. The emission contours in Figure 9 are seen to be qualitatively

very similar to those derived from the MWO photospheric field measurements (Figure 4). Since no BMRs were deposited above latitude $|L| = 30^\circ$ in this simulation, we conclude that the high-latitude enhancements originate from fields that were transported there from lower latitudes.

4. BUTTERFLY DIAGRAMS OF CORONAL EUV EMISSION

High-latitude enhancements are also seen on the disk in extreme-ultraviolet (EUV) images of the Sun. For example, Figure 10 shows the global distribution of Fe XII 19.5 nm and He II 30.4 nm emission during CR 2042 (starting date 2006 April 10), in the declining phase of cycle 23; these Carrington maps were assembled from the central meridian portions of full-disk EIT images. The high-latitude enhancements form an almost continuous band occupying the area between the polar crown filaments and the polar-hole boundary in each hemisphere. The band tends to be brightest at those longitudes where low-latitude active regions are present. It should be noted that, because of its finite extent in the radial direction, the optically thin Fe XII 19.5 nm emission tends to be further enhanced by projection effects (limb brightening).

In Figure 11, we display the butterfly diagrams of 19.5 nm and 30.4 nm emission for solar cycle 23 (CR 1905–1937, 1942–2089). Again, we have taken eleven-rotation running means and then subtracted from each column of pixels a 25° running mean in latitude. As expected, the patterns of locally enhanced emission resemble those found for the coronal green line.

5. CONCLUSIONS

Using both green-line simulations and EUV observations, we have constructed butterfly diagrams of coronal emission in order to determine the origin of the high-latitude enhancements that have been taken as evidence for an extended activity cycle lasting $\gtrsim 17$ yr. We find that the enhancements, which appear near the poles just after sunspot maximum and migrate equatorward through the declining phase of the cycle, are caused by the concentration of trailing-polarity flux toward the poles by meridional flow, and mark the strong-field footpoints of closed loops bordering the polar coronal holes. As the new cycle takes off and active regions with reversed north–south polarity orientation emerge at midlatitudes, the polar holes begin to close

down and their strongly enhanced borders (formerly occupied by open flux but now linked by closed loops to the trailing-polarity sectors of the active regions) recede poleward again. The high-latitude enhancements thus form a U-shaped structure centered at sunspot minimum. In most cases, a gap is present between the bottom of the U and the start of the low-latitude band representing the sunspot activity zone. This gap exists because the first active regions of the new cycle generally emerge well equatorward of the polar-hole boundaries.

In addition to the high- and low-latitude bands, we have noted the existence of a fragmentary emission structure occurring ~ 2 yr after the initial “rush to the poles” that cancels the old-cycle polar fields. This structure is cospatial with the surges of trailing-polarity flux that establish the new polar fields, and represents the actual birth of the high-latitude band, which should more properly be regarded as having a “ \sim ” rather than a simple “U” shape.

We conclude that the enhanced emission preceding the emergence of new-cycle sunspots reflects the activity of the ongoing cycle, rather than constituting part of an extended cycle. In particular, it does not represent the *in situ* emergence of new-cycle fields, but results from the poleward transport of trailing-polarity flux from the sunspot belts, which gives rise to concentrated polar fields ringed by closed loops with strong footpoint fields. We have confirmed this point by means of a flux transport simulation in which all of the BMRs are deposited in the sunspot latitudes; the resulting patterns of green-line emission are essentially the same as those derived from the observed photospheric fields (compare Figures 4 and 9).

The question of the relationship between torsional oscillations and enhanced coronal emission remains. The cycle 23 butterfly diagram of Howe et al. (2009), obtained by averaging helioseismic measurements between the two hemispheres, suggests that the equatorward-migrating zone of faster flows forms a continuous structure extending through the cycle minimum. Moreover, it is clear that the polar coronal holes cannot play a role in shaping the torsional oscillation patterns, as they do in truncating the coronal emission at high latitudes. Nevertheless, it is still possible that the butterfly diagram of torsional oscillations reflects the poleward transport of active-region fields to the poles, either through cross-talk between the Doppler and

magnetic signals, or through a direct or indirect physical interaction between the large-scale field and the near-surface flows. For example, the slower equatorward migration of the torsional oscillations during the declining phase of cycle 23 may reflect the weakness of the polar fields as compared with those in previous cycles; this weakness in turn reflects the fact that the net amount of trailing-polarity flux reaching the poles was smaller during cycle 23 (Schrijver & Liu 2008; Wang et al. 2009).

We are indebted to R. K. Ulrich (MWO) for making the photospheric field data used in this paper available. This work was funded by NASA and the Office of Naval Research.

REFERENCES

- Altrock, R., Howe, R., & Ulrich, R. 2008, in ASP Conf. Ser. 383, Subsurface and Atmospheric Influences on Solar Activity, ed. R. Howe, et al. (San Francisco, CA: ASP), 335
- Altrock, R. C. 1997, *Sol. Phys.*, 170, 411
- Benevolenskaya, E. E., Kosovichev, A. G., & Scherrer, P. H. 2001, *ApJ*, 554, L107
- Billings, D. E. 1966, A Guide to the Solar Corona (New York: Academic), 66
- Guhathakurta, M., Fisher, R. R., & Altrock, R. C. 1993, *ApJ*, 414, L145
- Guhathakurta, M., Rottman, G. J., Fisher, R. R., Orrall, F. Q., & Altrock, R. C. 1992, *ApJ*, 388, 633
- Howe, R., Christensen-Dalsgaard, J., Hill, F., Komm, R., Schou, J., & Thompson, M. J. 2009, *ApJ*, 701, L87
- Kirk, M. S., Pesnell, W. D., Young, C. A., & Hess Webber, S. A. 2009, *Sol. Phys.*, 257, 99
- LaBonte, B. J., & Howard, R. 1982, *Sol. Phys.*, 75, 161
- Legrand, J. P., & Simon, P. A. 1981, *Sol. Phys.*, 70, 173
- Leroy, J.-L., & Noens, J.-C. 1983, *A&A*, 120, L1
- Schrijver, C. J., & Liu, Y. 2008, *Sol. Phys.*, 252, 19
- Sheeley, N. R., Jr., Wang, Y.-M., & Harvey, J. W. 1989, *Sol. Phys.*, 119, 323
- Snodgrass, H. B. 1987, *Sol. Phys.*, 110, 35
- Spruit, H. C. 2003, *Sol. Phys.*, 213, 1
- Svalgaard, L., Duvall, T. L., Jr., & Scherrer, P. H. 1978, *Sol. Phys.*, 58, 225
- Ulrich, R. K., Bertello, L., Boyden, J. E., & Webster, L. 2009, *Sol. Phys.*, 255, 53
- Ulrich, R. K., Evans, S., Boyden, J. E., & Webster, L. 2002, *ApJS*, 139, 259
- Wang, Y.-M., Robbrecht, E., & Sheeley, N. R., Jr. 2009, *ApJ*, 707, 1372
- Wang, Y.-M., & Sheeley, N. R., Jr. 1995, *ApJ*, 447, L143
- Wang, Y.-M., et al. 1997, *ApJ*, 485, 419
- Wilson, P. R., Altrock, R. C., Harvey, K. L., Martin, S. F., & Snodgrass, H. B. 1988, *Nature*, 333, 748